Nano Research Energy

ISSN 2791-0091 CN 10-1944/O6
https://doi.org/10.26599/NRE.2026.9120270

Research Article

# Electronegativity-programmed N-B dipolar carbon nanofiber interlayers for spatially confined iodine redox in aqueous zinc-iodine batteries

Qi Xiang[1,2,§], Zhengqian Jin[2,§], Teng Deng[1,2,§], Yaowen Yue[1,2], Kai Li[2], Minghao Xie[2], Zekai Mei[3], Hongyang Zhao[2], Juan Wang[1](✉), Zhongxiao Song[3], Yangyang Liu[4](✉), Shujiang Ding[2], Kai Xi[1](✉)

[1] Shaanxi Key Laboratory of Nanomaterials and Nanotechnology, Xi'an Key Laboratory of Clean Energy, School of Mechanical & Electrical Engineering, Xi'an University of Architecture and Technology, Xi'an 710055, China

[2] School of Chemistry, Engineering Research Center of Energy Storage Materials and Devices, Ministry of Education, National Innovation Platform (Center) for Industry-Education Integration of Energy Storage Technology, State Key Laboratory of Electrical Insulation and Power Equipment, Engineering Research Center of Energy Storage Material and Chemistry, Universities of Shaanxi Province, Xi'an Jiaotong University, Xi'an 710049, China

[3] State Key Laboratory for Mechanical Behavior of Materials, Xi'an Jiaotong University, Xi'an 710049, China

[4] School of Instrument Science and Technology, Xi'an Jiaotong University, Xi'an 710049, China

[§] Qi Xiang, Zhengqian Jin, and Teng Deng contributed equally to this work.

*Nano Research Energy*, **Just Accepted Manuscript** • https://doi.org/10.26599/NRE.2026.9120270
https://www.sciopen.com/journal/2791-0091 on Sep. 17, 2026



## Just Accepted

# Table of contents

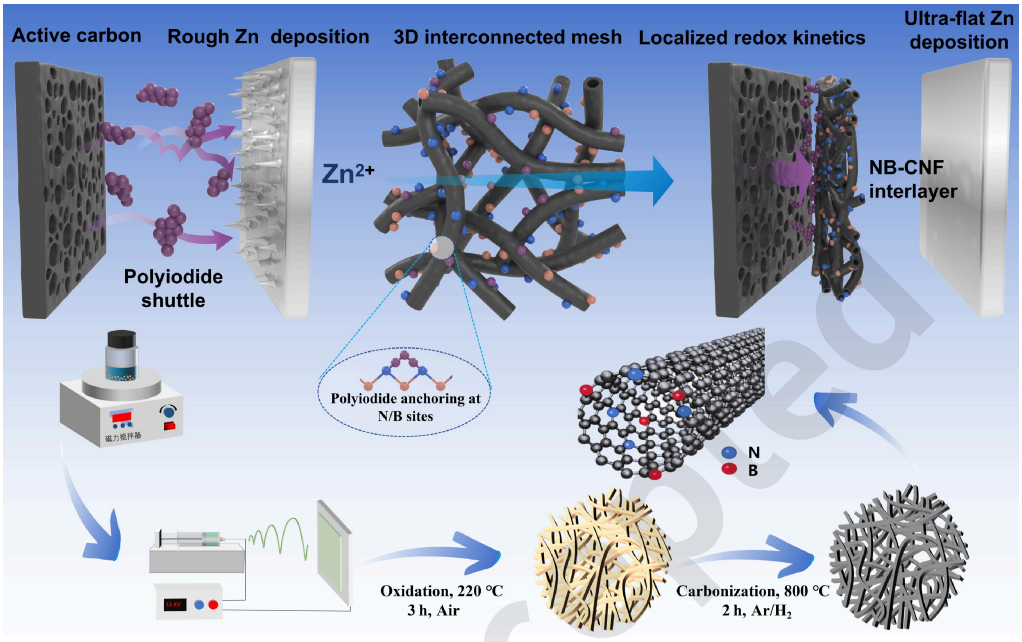


Electronegativity-programmed N/B co-doped carbon nanofibers spatially confine polyiodide intermediates within an electrochemically accessible redox field. This regulation suppresses iodine crossover, accelerates interfacial conversion, and stabilizes Zn plating/stripping for durable aqueous Zn–$I_2$ batteries.

Nano Research Energy

ISSN 2791-0091 (print); 2790-8119 (online)
https://doi.org/10.26599/NRE.2026.9120270

Research Article

# Electronegativity-programmed N-B dipolar carbon nanofiber interlayers for spatially confined iodine redox in aqueous zinc-iodine batteries

Qi Xiang[1,2,§], Zhengqian Jin[2,§], Teng Deng[1,2,§], Yaowen Yue[1,2], Kai Li[2], Minghao Xie[2], Zekai Mei[3], Hongyang Zhao[2], Juan Wang[1] (✉), Zhongxiao Song[3], Yangyang Liu[4] (✉), Shujiang Ding[2], and Kai Xi[1] (✉)

[1] *Shaanxi Key Laboratory of Nanomaterials and Nanotechnology, Xi'an Key Laboratory of Clean Energy, School of Mechanical & Electrical Engineering, Xi'an University of Architecture and Technology, Xi'an 710055, China*

[2] *School of Chemistry, Engineering Research Center of Energy Storage Materials and Devices, Ministry of Education, National Innovation Platform (Center) for Industry-Education Integration of Energy Storage Technology, State Key Laboratory of Electrical Insulation and Power Equipment, Engineering Research Center of Energy Storage Material and Chemistry, Universities of Shaanxi Province, Xi'an Jiaotong University, Xi'an 710049, China*

[3] *State Key Laboratory for Mechanical Behavior of Materials, Xi'an Jiaotong University, Xi'an 710049, China*

[4] *School of Instrument Science and Technology, Xi'an Jiaotong University, Xi'an 710049, China*

[§] *Qi Xiang, Zhengqian Jin, and Teng Deng contributed equally to this work.*

**Received:** 26 July 2026 / **Revised:** 24 August 2026 / **Accepted:** 11 September 2026

## ABSTRACT

Aqueous zinc-iodine ($Zn-I_2$) batteries are promising candidates for safe and low-cost energy storage; however, their operation is severely limited by the uncontrolled migration of soluble polyiodide intermediates. Beyond the conventional shuttle effect, this challenge arises from the spatial delocalization of iodine redox chemistry, where $I^-/I_3^-/I_5^-$ species propagate from the cathode and trigger electrochemical crosstalk with the Zn anode. Here, inspired by electronegativity-driven activation of heteroatom-doped carbon catalysts, we propose an electronegativity-programmed strategy for iodine-redox-field engineering using self-standing nitrogen–boron co-doped carbon nanofiber (NB-CNF) interlayers. The lower electronegativity of B and higher electronegativity of N relative to C induce charge-asymmetric N/B environments with dipolar character that serve as polar anchoring centers for iodine species, while the superwettable, conductive nanofiber network further integrates the immobilized intermediates into a spatially confined interfacial redox field. This design transforms bulk-diffusion-dominated iodine chemistry into a spatially regulated surface-confined and spatially regulated reaction process. The resulting redox-field confinement suppresses iodine-induced Zn degradation, enabling a smooth Zn surface with reduced roughness and stable Zn symmetric-cell cycling over 1,200 h. Consequently, $Zn-I_2$ full cells deliver excellent rate capability, with the capacity at 50 C reaching 1.8 times that of pristine carbon nanofiber controls, 87% capacity retention after 48 h resting, and stable cycling over 10,000 cycles at 10 C. This work extends $Zn-I_2$ battery design from molecular confinement to electronegativity-programmed spatial engineering of electrochemical redox fields.

## KEYWORDS

aqueous $Zn–I_2$ batteries, electronegativity-programmed interfaces, N–B dipolar carbon, iodine redox-field confinement, polyiodide crosstalk, zinc anode stabilization

## 1 Introduction

The rapid deployment of renewable electricity has created an urgent demand for energy-storage systems that combine low cost, intrinsic safety and long-term durability [1–5]. Aqueous zinc-iodine batteries ($Zn-I_2$) are attractive candidates because they couple the abundance and safety of zinc (Zn) metal with the high theoretical capacity, fast redox kinetics and low cost of iodine chemistry [6, 7]. These features make $Zn-I_2$ batteries particularly appealing for grid-scale storage, where material availability, operational safety and long cycle life are more decisive than gravimetric energy density alone. However, practical $Zn-I_2$ batteries still lag behind their theoretical promise because iodine redox chemistry proceeds through soluble intermediates [8]. The solution-mediated nature of $I^-/I_3^-/I_5^-$ conversion enables rapid kinetics, but it also allows active redox species to leave the cathode region and redistribute across the cell [9]. The resulting spatial



Address correspondence to Juan Wang, juanwang618@126.com; Yangyang Liu, liuyy0510@xjtu.edu.cn; Kai Xi, kx210.cam@xjtu.edu.cn

instability converts a cathode-side kinetic advantage into a whole-cell degradation pathway.

In conventional Zn-$I_2$ configurations, soluble $I^-/I_3^-/I_5^-$ redox couples are not confined to the cathode region [10–12]. Instead, they diffuse through the electrolyte and progressively extend the iodine reaction zone toward the Zn anode [13, 14], causing active iodine loss, self-discharge [15–17], Zn corrosion, surface passivation and dendrite formation [18–23]. Although this degradation is commonly described as the polyiodide shuttle effect [24], such a description only captures the movement of soluble species. The deeper problem is the loss of spatial control over iodine redox chemistry [25]. Once the iodine redox field becomes delocalized, cathode reactions are no longer isolated from the anode, and the two electrodes become coupled through parasitic chemical and electrochemical pathways [26–28]. Therefore, suppressing polyiodide migration is not sufficient by itself; durable Zn–$I_2$ batteries require control over the spatial position, electronic connectivity and reversibility of the iodine reaction field [29–32].

Heteroatom doping (HD) offers a powerful route to activate metal-free carbon interfaces because it redistributes electron density through electronegativity differences [33–36]. In a carbon lattice, N is more electronegative than C and tends to withdraw electron density, whereas B is less electronegative and behaves as an electron-deficient/Lewis-acidic component [37]. Their co-incorporation can therefore break the electronic symmetry of the carbon skeleton and induce local electronic polarization consistent with a dipolar environment rather than merely increasing defect density [38–40]. This principle has been widely exploited in metal-free carbon electrocatalysis, where electronegativity-driven charge polarization creates active centers for molecular adsorption and electron transfer [41–44]. Transferring this concept to Zn–$I_2$ batteries suggests a more fundamental interlayer design strategy: an electronegativity-programmed carbon interface could selectively polarize and anchor highly polarizable iodine species, while a continuous conductive framework keeps these immobilized intermediates electrochemically accessible [45–47].

Here we propose iodine redox-field engineering as a field-level design principle for aqueous Zn-$I_2$ batteries and realize it with self-standing nitrogen–boron co-doped carbon nanofibers (NB-CNFs) prepared by electrospinning (ES), preoxidation (PO) and carbonization. Iodine redox-field confinement refers to spatially restricting soluble iodine intermediates within an electrochemically accessible cathode/interlayer region while maintaining their reversible redox conversion. The charge-asymmetric N–B sites generated by electronegativity contrast provide polar anchoring centers for $I^-/I_3^-$ intermediates, while the interconnected nanofiber membrane provides continuous electron pathways, rapid electrolyte wetting and mechanical conformability [48–50]. In this framework, the interlayer is not a passive adsorbent or blocking membrane, but an electronegativity-programmed dipolar interface that pins the migrating polyiodide front before it reaches the Zn anode, thereby converting uncontrolled liquid-phase iodine chemistry into a confined interfacial redox process. H-type diffusion, ultraviolet-visible spectroscopy (UV-Vis), density functional theory (DFT) calculations, electrochemical kinetic analysis, self-discharge measurements, Zn-anode characterization and full-cell cycling collectively demonstrate that this strategy suppresses cathode-anode crosstalk, stabilizes Zn plating/stripping and improves long-term Zn–$I_2$ battery performance.

## 2 Results and discussion

### 2.1 Construction of an electronegativity-programmed N–B dipolar nanofiber interlayer

Figure 1(a) schematically illustrates the use of a self-standing NB-CNF interlayer to spatially confine iodine redox chemistry, while the detailed electrospinning-preoxidation-carbonization route is provided in Fig. S1 in the Electronic Supplementary Material (ESM). Polyacrylonitrile (PAN) was used as the carbon precursor, while urea and boric acid served as nitrogen and boron sources, respectively. The mixed precursor was processed into a continuous nanofiber membrane by electrospinning, followed by preoxidation at 220 °C to stabilize the polymer chains through cyclization and cross-linking. Thermal analysis (TA) of the CNF and NB-CNF precursors further confirms their thermal-transition behavior during stabilization and subsequent carbonization (Fig. S5 in the ESM). Subsequent carbonization at 800 °C under an $Ar/H_2$ atmosphere converted the polymer skeleton into a conductive carbon network while incorporating nitrogen and boron atoms into the carbon framework. The resulting NB-CNF membrane preserves the one-dimensional interconnected morphology of pristine carbon nanofibers but shows rougher surfaces (Figs. 1(b)–1(e)). This fibrous architecture is essential for redox-field engineering because it combines electrolyte-accessible channels, continuous electron pathways and sufficient interfacial area for dipolar anchoring. Elemental mapping confirms the homogeneous distribution of N and B throughout the nanofibers, indicating that charge-polarized sites are spatially dispersed across the interlayer rather than locally aggregated (Fig. 1(f)). At the macroscopic scale, the NB-CNF membrane is self-standing and flexible, maintaining mechanical integrity under bending and enabling intimate contact with the electrode surface (Fig. 1(g) and Fig. S2 in the ESM). Thus, NB-CNF integrates molecular dipolar sites, mesoscopic ion channels and macroscopic conformability into a single electronegativity-programmed redox-field-regulating interlayer.

### 2.2 Electronegativity-derived local charge asymmetry in N–B co-doped carbon frameworks

The structural and chemical characteristics of NB-CNF were examined to clarify how electronegativity contrast generates local charge asymmetry. X-ray diffraction (XRD) patterns show broad diffraction peaks around $2\theta \approx 25°$, corresponding to disordered graphitic carbon, without detectable impurity phases (Fig. 2(a)), indicating that N–B doping modifies the local electronic environment without destroying the carbon framework. Fourier-transform infrared spectroscopy (FTIR) spectra show characteristic signals associated with B–N, C=N and C=C bonding environments, confirming stable heteroatom-containing carbon structures (Fig. 2(b)). Raman spectra reveal a slightly increased $I_D/I_G$ ratio for NB-CNF compared with CNF, suggesting that heteroatom incorporation creates additional defect/edge sites that can participate in interfacial charge regulation (Fig. 2(c)). X-ray photoelectron spectroscopy (XPS) analysis further confirms the coexistence of B and N species in the carbon network. The survey spectrum confirms the emergence of the B 1s signal in NB-CNF, while N 1s signals are observed in both CNF and NB-CNF owing to the PAN-derived nitrogen-containing carbon framework (Fig. 2(e)). High-resolution spectra show C–N, B–C/B–O and multiple nitrogen configurations, including pyridinic and graphitic

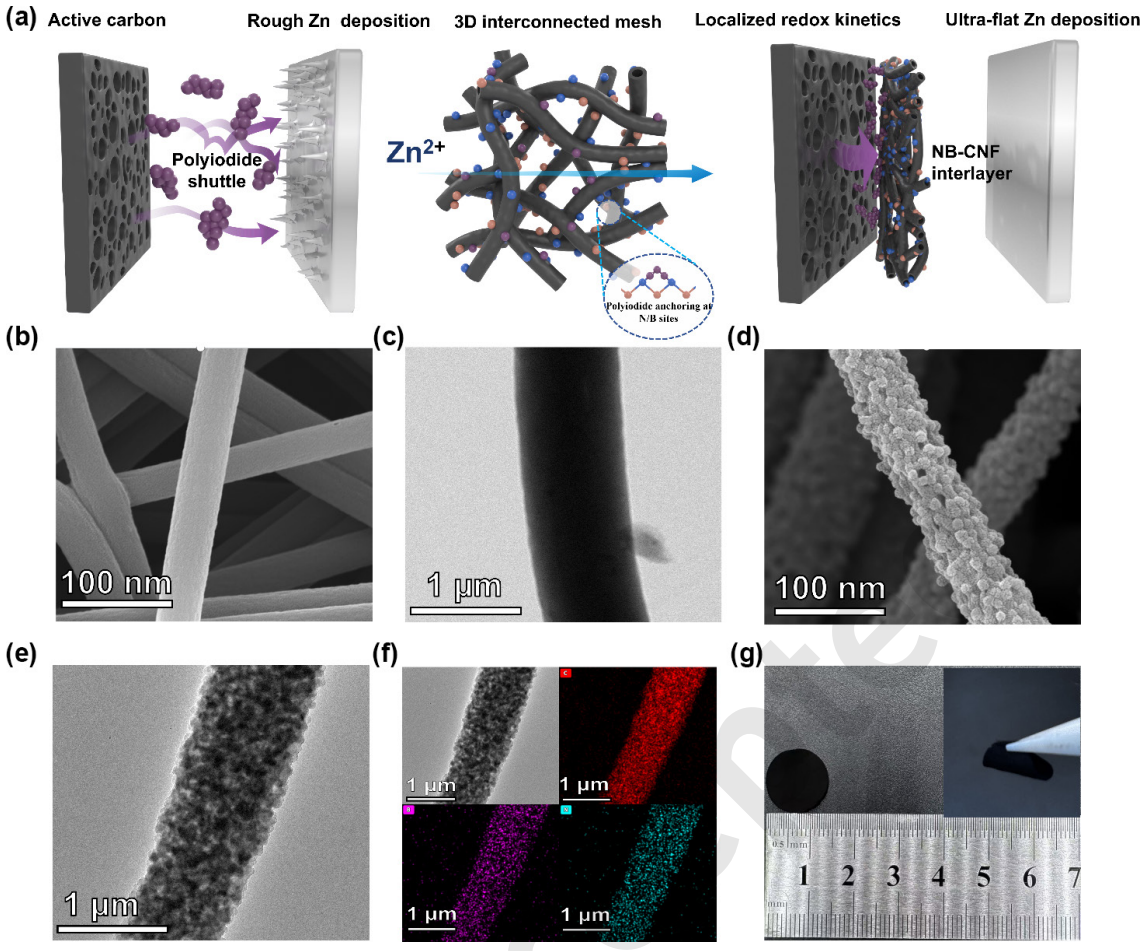


**Figure 1** Construction of the electronegativity-programmed NB-CNF interlayer. (a) Schematic illustration comparing uncontrolled polyiodide migration and rough Zn deposition in a conventional Zn–I2 cell with spatially confined iodine redox chemistry and uniform Zn deposition enabled by the NB-CNF interlayer. (b, c) SEM and TEM images of pristine CNF. (d, e) SEM and TEM images of NB-CNF. (f) Elemental mapping images of NB-CNF, showing homogeneous N and B distributions. (g) Photograph of the flexible self-standing NB-CNF membrane.

nitrogen species (Figs. 2(f)–2(i)). Since B is less electronegative than C whereas N is more electronegative, adjacent B/N environments polarize the surrounding carbon lattice, giving rise to locally polarized environments consistent with dipolar character. The N–B co-doped carbon framework can therefore be viewed not simply as a defect-rich adsorbent, but as an electronegativity-programmed polarized surface that creates spatial anchoring centers for iodine intermediates while preserving electronic conduction along the nanofiber skeleton.

### 2.3 Spatial pinning of the polyiodide redox field by dipolar anchoring sites

To evaluate whether the electronegativity-programmed NB-CNF interlayer can regulate the spatial propagation of iodine species, H-type diffusion experiments were conducted. In the control configuration without an effective NB-CNF interlayer, the electrolyte in the opposite chamber gradually turned yellow within 60 min, indicating continuous migration of soluble polyiodide species (Figs. 3(a)–3(d)). In contrast, after introducing the NB-CNF interlayer, the opposite chamber remained nearly colorless during the same period (Figs. 3(e)–3(h)). This visual contrast indicates that NB-CNF does not merely delay molecular diffusion; rather, it strongly restricts the outward propagation of polyiodide species. UV-Vis spectra further quantify this diffusion-suppression effect. For the NB-CNF-containing system, the characteristic absorption peaks of $I_3^-$ at approximately 290 and 360 nm remain nearly undetectable over time, whereas the CNF control shows progressively intensified $I_3^-$ absorption (Figs. 3(i) and 3(j)). Importantly, time-resolved contact-angle measurements show that electrolyte droplets rapidly spread on NB-CNF within 100 ms, approaching complete wetting (Fig. 3(k)). Thus, the interlayer functions as an open and wettable reaction field rather than a dense blocking membrane: polyiodide propagation is spatially confined, while electrolyte infiltration and ion transport remain accessible. DFT calculations further clarify the molecular basis of this redox-field pinning. Compared with N-doped carbon sites, N/B co-doping induces a site- and species-dependent redistribution of iodine adsorption, selectively strengthening $I^-$ adsorption at pyridinic N/B sites and $I_3^-$ adsorption at pyrrolic N/B sites. Boron co-doping enhances the adsorption energy of pyridinic-N sites toward $I^-$ from −6.72 to −7.38 eV and strengthens the interaction of pyrrolic-N sites toward $I_3^-$ from −3.70 to −3.97 eV (Fig. 3(l) and Fig. S3 in the ESM). These comparisons indicate that the N-containing sites provide the primary iodine-interaction environments, whereas B incorporation modifies the local electronic structure of the neighboring N/C framework and strengthens iodine adsorption in a site-dependent manner. Accordingly, the enhanced interactions with $I^-$ and $I_3^-$ are attributed to the cooperative electronic environment of neighboring N/B motifs rather than to an independently identified B adsorption site. These results suggest

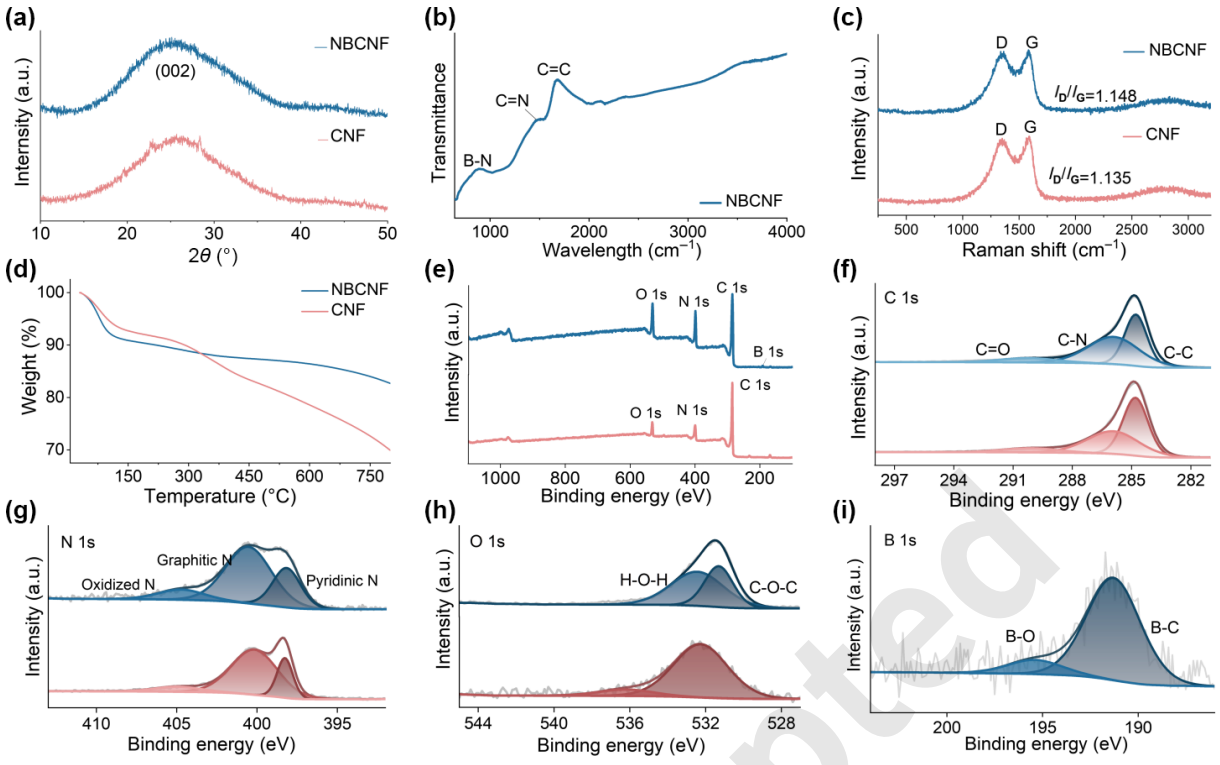


**Figure 2** Structural and chemical characterization of NB-CNF and CNF. (a) XRD patterns of NB-CNF and CNF. (b) FTIR spectrum of NB-CNF. (c) Raman spectra of NB-CNF and CNF. (d) TGA curves of NB-CNF and CNF. (e) XPS survey spectra of NB-CNF and CNF. (f) High-resolution C 1s spectra of NB-CNF and CNF. (g) High-resolution N 1s spectra of NB-CNF and CNF. (h) High-resolution O 1s spectra of NB-CNF and CNF. (i) High-resolution B 1s spectrum of NB-CNF.

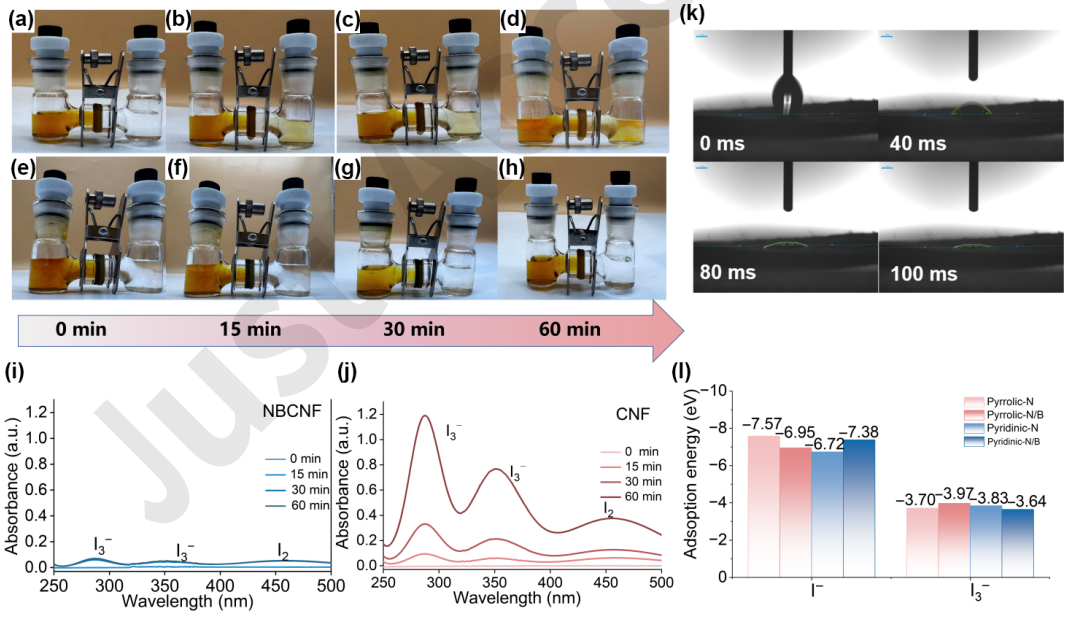


**Figure 3** Polyiodide confinement and iodine-species adsorption on NB-CNF. (a–d) Time-dependent H-cell diffusion photographs of the CNF control at 0, 15, 30, and 60 min, respectively. (e–h) Time-dependent H-cell diffusion photographs of the NB-CNF interlayer at 0, 15, 30, and 60 min, respectively. (i) UV–Vis spectra of the receiving chamber with the NB-CNF interlayer. (j) UV–Vis spectra of the receiving chamber with the CNF control. (k) Time-resolved contact-angle images of NB-CNF. (l) Calculated adsorption energies of $I^-$ and $I_3^-$ on N-doped and N/B co-doped carbon sites.

that N–B-induced local polar environments anchor iodine intermediates and help confine the redox front at a conductive interface instead of allowing iodine species to propagate freely through the electrolyte. The corresponding total density of states (TDOS) results further indicate that N/B co-doping modulates the local electronic structure of the carbon framework, which is consistent with the formation of electronically polarized adsorption sites (Fig. S4 in the ESM).

### 2.4 Wiring the pinned iodine redox field into fast interfacial conversion

Pinning the polyiodide field alone is insufficient if the immobilized iodine species cannot be rapidly converted. The electrochemical behavior of the NB-CNF interlayer was therefore investigated by cyclic voltammetry (CV) and impedance analysis. At 0.2 mV·s$^{-1}$, the NB-CNF-based cell exhibits higher redox peak currents,

sharper peak profiles and smaller peak separation than the CNF control (Fig. 4(a)), indicating improved reversibility and reduced polarization. When the scan rate increases from 0.2 to 1.0 mV·s$^{-1}$, the NB-CNF electrode maintains well-defined redox peaks with limited potential shift, whereas the CNF control shows more pronounced peak distortion and polarization (Figs. 4(b) and 4(c)). These results indicate that the iodine redox field pinned at NB-CNF remains electrochemically accessible under fast charge–discharge conditions. Capacitive contribution analysis provides additional evidence for enhanced interfacial kinetics and reduced diffusion limitation. The NB-CNF system displays an increasing capacitive-controlled contribution with increasing scan rate, rising from 75% at 0.2 mV·s$^{-1}$ to 87% at 1.0 mV·s$^{-1}$ (Fig. 4(d)). This increasing capacitive-controlled contribution suggests that a larger fraction of iodine conversion proceeds through fast interfacial processes rather than being governed solely by bulk diffusion of soluble intermediates. Electrochemical impedance spectroscopy (EIS) shows that NB-CNF markedly reduces charge-transfer resistance and ion-diffusion impedance compared with CNF (Fig. 4(e)). Four-point probe measurements further reveal lower resistivity and smaller positional fluctuations across the NB-CNF membrane (Fig. 4(f)), confirming that the fibrous network provides a spatially uniform conductive scaffold. These results demonstrate that the electronegativity-programmed interlayer not only immobilizes the polyiodide field but also wires the pinned intermediates into the external circuit, converting migrating polyiodides from parasitic species into electronically connected interfacial redox participants.

## 2.5 Decoupling Zn-anode degradation from the iodine redox field

The effect of NB-CNF on Zn-anode stability was examined to verify whether iodine redox-field confinement can suppress anode-side degradation. After cycling under the tested Zn-$I_2$ cell conditions, atomic force microscopy (AFM) analysis shows that the Zn anode paired with NB-CNF maintains a relatively smooth surface with a roughness of $R_a$ = 1.284 μm (Fig. 5(a)). In contrast, the Zn anode from the CNF-based cell displays pronounced protrusions and dendritic features, with a much higher roughness of $R_a$ = 4.103 μm (Fig. 5(b)). The corresponding roughness profiles further confirm the more homogeneous Zn surface in the NB-CNF system (Fig. 5(c)). Scanning electron microscopy (SEM) images of Zn anodes after the same cycling protocol show a dense and uniform morphology with NB-CNF, whereas the CNF control exhibits a rough and porous dendritic surface (Figs. 5(e) and 5(g)). These differences indicate that NB-CNF stabilizes the Zn anode not simply by serving as a mechanical buffer, but also by reducing the exposure of the Zn surface to migrating iodine species. When polyiodide intermediates propagate to the anode side, they can induce parasitic redox reactions, corrosion, passivation and nonuniform Zn plating. By pinning iodine intermediates within the interfacial redox field, NB-CNF reduces the chemical exposure of the Zn anode to soluble iodine species and thereby mitigates surface roughening and dendrite formation. Zn symmetric-cell tests were further used to evaluate the direct interfacial effect of NB-CNF on Zn plating/stripping in the absence of iodine species. The NB-CNF-containing symmetric cell operates stably for more than 1200 h at 1 mA·cm$^{-2}$ and 1 mAh·cm$^{-2}$, while maintaining stable voltage profiles even under harsher conditions of 5 mA·cm$^{-2}$ and 5 mAh·cm$^{-2}$ (Figs. 5(d) and 5(f)). In comparison, the CNF control shows evident voltage fluctuations from the early stage. These results indicate that NB-CNF can directly regulate Zn plating/stripping at the Zn interface. This direct interfacial effect is distinct from the protection observed in Zn–$I_2$ full cells, where suppression of polyiodide crossover reduces the chemical exposure of the Zn anode.

## 2.6 Electrochemical consequences of iodine redox-field engineering

After demonstrating the spatial confinement of iodine species and improved Zn-anode stability with NB-CNF, the full-cell electrochemical performance was evaluated. Rate-performance

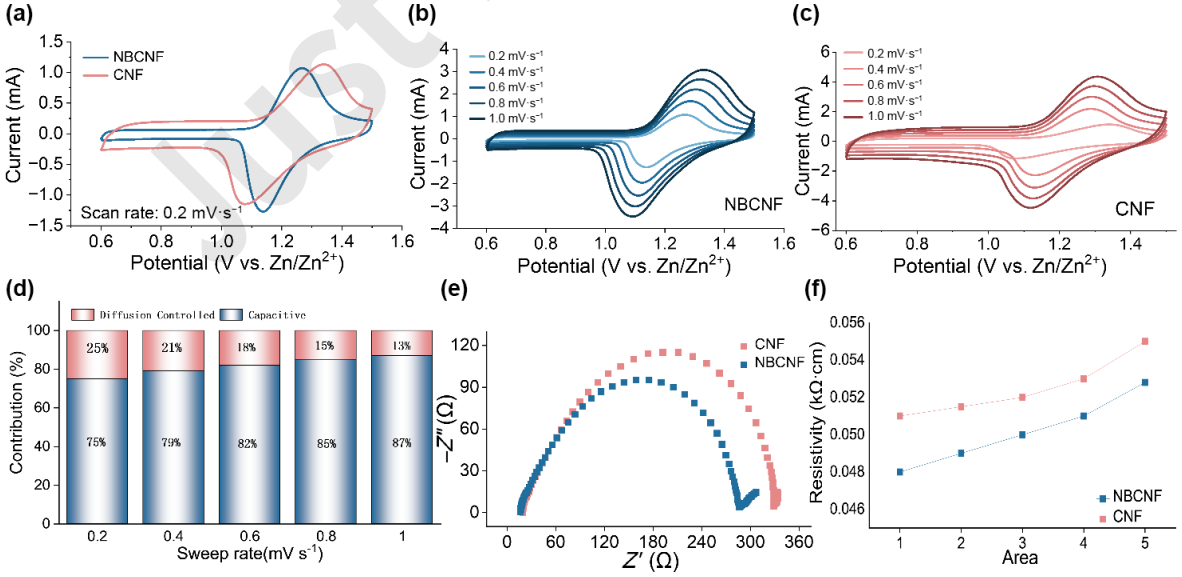


**Figure 4** Electrochemical kinetics of iodine conversion with NB-CNF and CNF at room temperature. (a) CV curves of NB-CNF and CNF cells at 0.2 mV·s$^{-1}$ within 0.6–1.6 V. (b, c) Scan-rate-dependent CV curves of the NB-CNF and CNF cells, respectively, from 0.2 to 1.0 mV·s$^{-1}$ within 0.6–1.6 V. (d) Capacitive-controlled and diffusion-controlled current contributions of the NB-CNF cell at different scan rates, calculated from the scan-rate-dependent CV data using $i(V)=k_1v+k_2v^{1/2}$, where $k_1v$ and $k_2v^{1/2}$ represent the capacitive-controlled and diffusion-controlled contributions, respectively. (e) EIS spectra of NB-CNF and CNF cells measured at open-circuit voltage over 100 kHz–0.01 Hz with a perturbation amplitude of 5 mV. (f) Resistivity profiles of NB-CNF and CNF membranes measured by the four-point probe method.

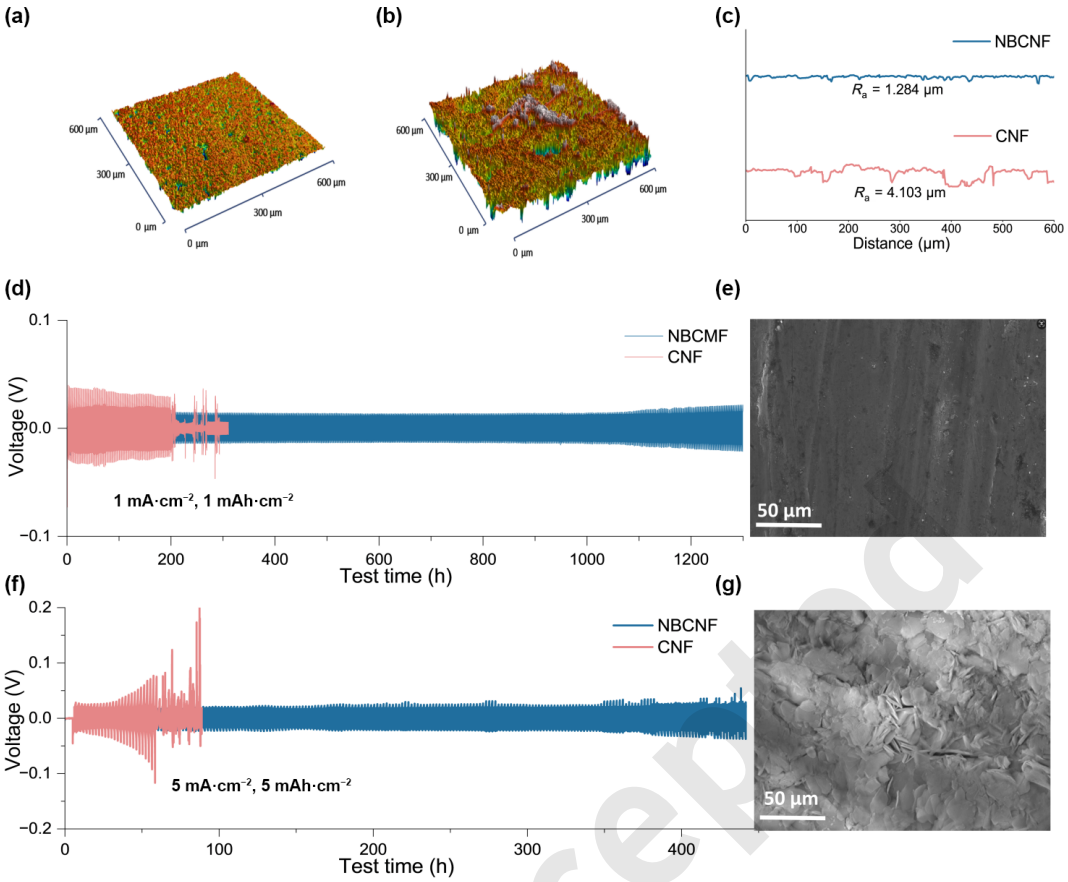


**Figure 5** Zn-anode stabilization with NB-CNF and CNF interlayers. (a, b) AFM topographies of Zn anodes cycled with NB-CNF and CNF, respectively. (c) Corresponding roughness profiles of the cycled Zn anodes. (d) Galvanostatic Zn plating/stripping profiles of Zn//Zn symmetric cells with NB-CNF and CNF interlayers at 1 mA·cm$^{-2}$ with an areal capacity of 1 mAh·cm$^{-2}$. (e) SEM image of the Zn surface cycled with NB-CNF, showing a relatively smooth and compact morphology. (f) Galvanostatic Zn plating/stripping profiles at 5 mA·cm$^{-2}$ with an areal capacity of 5 mAh·cm$^{-2}$. (g) SEM image of the Zn surface cycled with CNF, showing rough and flake-like Zn deposition. The symmetric-cell measurements were conducted at room temperature in 2 M $ZnSO_4$ aqueous electrolyte.

tests show that the NB-CNF-based cell delivers higher capacities over a wide range of rates from 1 to 50 C (Figs. 6(a) and 6(b)). At 50 C, the capacity of the NB-CNF system reaches 1.8 times that of the CNF control, and the capacity recovers well when the current rate is returned to lower values. This high-rate capability is consistent with the formation of a conductive and wettable interfacial redox field, where iodine intermediates are spatially localized but remain electrochemically active. Galvanostatic charge–discharge profiles further show that the NB-CNF system exhibits more stable plateaus and smaller voltage polarization than the CNF control at different current densities (Figs. 6(c) and 6(d)). This reduced polarization reflects more reversible iodine conversion within the confined interfacial field. More importantly, self-discharge tests demonstrate a marked improvement in iodine retention. After resting for 48 h in the charged state, the NB-CNF-based cell retains 87% of its capacity, whereas the CNF-based cell retains only 84% (Figs. 6(e) and 6(f)). This result is consistent with reduced polyiodide crossover and suppressed cathode–anode crosstalk. At 1 C, the NB-CNF cell delivers an initial capacity of approximately 200 mAh·g$^{-1}$ and maintains over 97% capacity retention after 500 cycles, with Coulombic efficiency (CE) remaining close to 100% (Fig. 6(g)). Long-term cycling further confirms the stability of the engineered iodine field. At 10 C, the NB-CNF-based cell maintains more than 80% capacity retention after 10,000 cycles, while the CNF control suffers short-circuit failure after 5,600 cycles (Fig. 6(h)). These results show that the benefit of NB-CNF does not arise from a simple increase in adsorption strength. Instead, electronegativity-programmed charge asymmetry reorganizes iodine chemistry spatially: the redox field is confined near the cathode/interlayer region, connected to a conductive scaffold and prevented from propagating toward the Zn anode.

## 3 Conclusion

In summary, this work redefines the degradation of aqueous Zn–$I_2$ batteries from a conventional polyiodide-shuttle problem to the spatial delocalization of the iodine redox field, and further demonstrates that this field can be regulated by electronegativity-programmed carbon interfaces. A self-standing N–B co-doped carbon nanofiber interlayer was designed as a dipolar redox-field regulator. The electronegativity contrast between B, C and N generates charge-asymmetric N–B sites that anchor $I^-/I_3^-/I_5^-$ intermediates, while the continuous conductive fibrous network wires these species into a confined interfacial reaction zone. This design spatially pins the polyiodide front while preserving electrolyte wetting, ion transport and electron conduction. As a result, confinement of iodine species reduces the exposure of the Zn anode to soluble iodine intermediates, thereby mitigating surface roughening, dendritic growth and long-term voltage instability. This anode-level stabilization further enables improved full-cell behavior, including enhanced high-rate capability, suppressed self-discharge and extended cycling stability. More broadly, this study establishes electronegativity-programmed

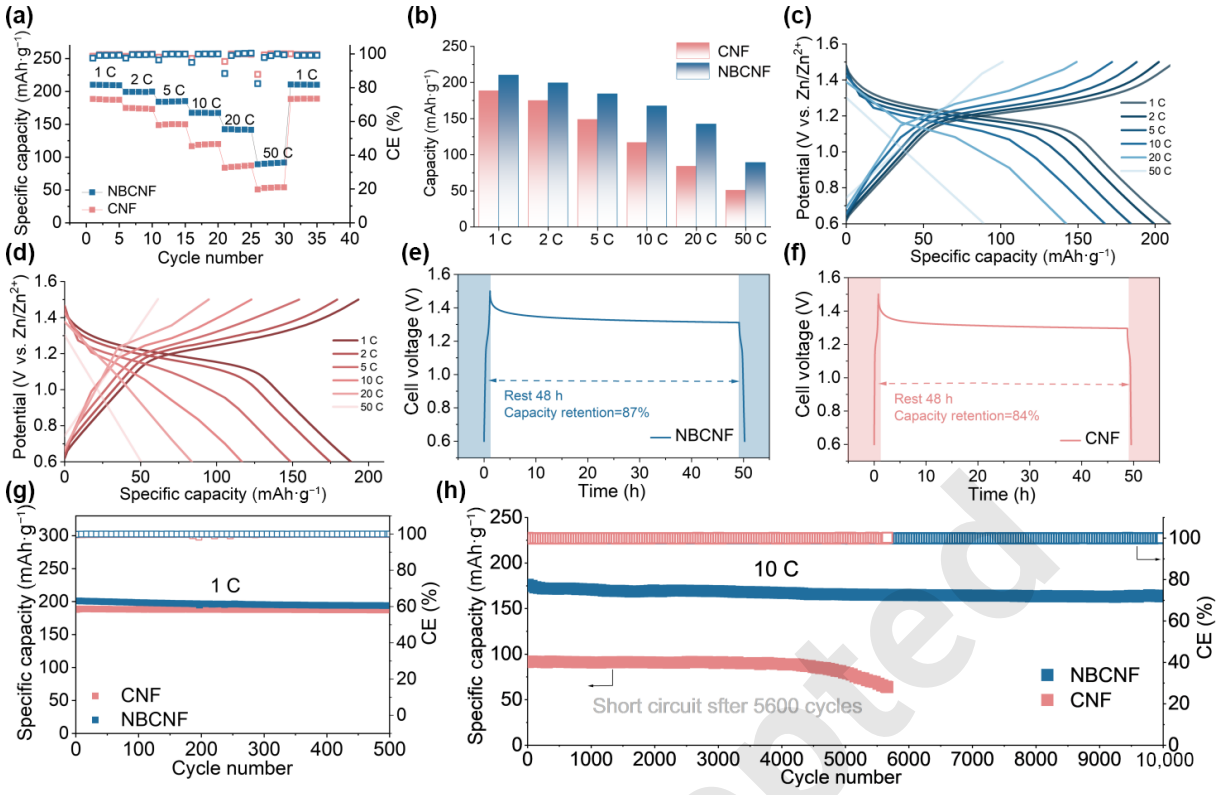


**Figure 6** Electrochemical consequences of electronegativity-programmed iodine redox-field engineering in Zn–$I_2$ full cells at room temperature. (a) Rate performance and Coulombic efficiency of Zn–$I_2$ cells with NB-CNF and CNF interlayers from 1 to 50 C. (b) Capacity comparison of NB-CNF and CNF cells at different rates. (c, d) Galvanostatic charge–discharge profiles of the NB-CNF and CNF cells, respectively, at different rates within 0.6–1.6 V. (e, f) Self-discharge profiles of the NB-CNF and CNF cells, respectively; the cells were charged to 1.6 V, rested for 48 h, and subsequently discharged to evaluate capacity retention. (g) Long-term cycling performance of NB-CNF and CNF cells at 1 C. (h) Long-term cycling performance of NB-CNF and CNF cells at 10 C. All specific capacities and C-rates were calculated based on the mass of iodine, with 1 C corresponding to 211 mA·g$^{-1}$.

iodine redox-field engineering as a design principle for aqueous metal–halogen batteries, shifting the focus from stronger molecular adsorption to spatial control of electrochemical reaction fields.

## Acknowledgements

Q.X., Z.J., and T.D. contributed equally to this work. The authors gratefully acknowledge the institutional support of the Shaanxi Key Laboratory of Nanomaterials and Nanotechnology and the Xi'an Key Laboratory of Clean Energy. Financial support for this work was provided by the National Natural Science Foundation of China (Grant Nos. 52471091, 22179036, 22278329 and 92472124), the Key Industrial Chain Project of Shaanxi Province (Grant Nos. 2023-ZDLGY-24 and 2024GX ZDCYL-04-07), the Yulin Science and Technology Bureau Project (Grant No. 2024-KJZG-QZZL 002), the Natural Science Basic Research Program of Shaanxi (Grant No. 2026JC-JCQN-076, 2026JC-QYCX-015), the Key Research and Development Program of Shaanxi Province (Grant No. 2024GX-YBXM 337), the Xi'an Science and Technology Plan Project (Grant No. 24GXFW0039), and the Open Foundation of State Key Laboratory for Advanced Metals and Materials. The High-Level Innovation and Entrepreneurship Talent Project of Qinchuangyuan (No. QCYRCXM-2022-308), and the State Key Laboratory for Electrical Insulation and Power Equipment (No. EIPE23125). The authors sincerely thank the faculty at the National Innovation Platform for Industry-Education Integration of Energy Storage Technology of Xi'an Jiaotong University—especially Mr. Geng Zhi for assistance—as well as staff at the Instrumental Analysis Center of Xi'an Jiaotong University.

## Declaration of conflicting interests

The authors declare no conflicting interests regarding the content of this article.

## Data availability

All data needed to support the conclusions in the paper are presented in the manuscript and the Supplementary Materials. Additional data related to this paper may be requested from the corresponding author upon request.

**Electronic Supplementary Material:** Supplementary material (please send us a short summary regarding the Supporting info, thanks) is available in the online version of this article at https://doi.org/10.26599/NRE.2026.9120270.

## References

[1] Xiao, T.; Yang, J. L.; Chao, D. L.; Fan, H. J. Multimodal electrolyte architecting for static aqueous zinc-halogen batteries. *Natl. Sci. Rev.* **2025**, *12*, nwaf029.

[2] She, L. N.; Cheng, H.; Yuan, Z. Y.; Shen, Z. Y.; Wu, Q.; Zhong, W.; Zhang, S. C.; Zhang, B.; Liu, C. W.; Zhang, M. C. et al. Rechargeable aqueous zinc-halogen batteries: Fundamental mechanisms, research issues, and future perspectives. *Adv. Sci.* **2024**, *11*, 2305061.

[3] Wen, H. K.; Wen, H. Y.; Sun, Y.; Li, J. Z.; Zhuang, C. L.; Liu, M.

H.; Li, H.; Fan, H.; Yin, B. S.; Zhang, S. W. et al. The frontiers of aqueous zinc-iodine batteries: A comprehensive review on mechanisms, optimization, and industrial prospects. *Adv. Funct. Mater.* **2025**, *35*, 2500323.

[4] Chen, H.; Li, X.; Fang, K. Q.; Wang, H. Y.; Ning, J. Q.; Hu, Y. Aqueous zinc-iodine batteries: From electrochemistry to energy storage mechanism. *Adv. Energy Mater.* **2023**, *13*, 2302187.

[5] Lin, D.; Li, Y. Recent advances of aqueous rechargeable zinc-iodine batteries: Challenges, solutions, and prospects. *Adv. Mater.* **2022**, *34*, 2108856.

[6] Jiang, Z. Y.; Yang, X.; Zhang, J.; Yang, J. S.; Sun, B. W.; Sun, Z. Q.; Xue, J. J.; He, J. H.; Sun, Z. X.; Liu, H. K. et al. From conventional two-electron to emerging multi-electron zinc-iodine batteries: Advantages, challenges, and future perspectives. *Adv. Funct. Mater.* **2025**, *35*, e11754.

[7] Pan, H. L.; Li, B.; Mei, D. H.; Nie, Z. M.; Shao, Y. Y.; Li, G. S.; Li, X. S.; Han, K. S.; Mueller, K. T.; Sprenkle, V. et al. Controlling solid-liquid conversion reactions for a highly reversible aqueous zinc-iodine battery. *ACS Energy Lett.* **2017**, *2*, 2674–2680.

[8] Yi, Z. H.; Cai, D. Q.; Fan, H. J. Rethinking the four-electron iodine redox mechanism in Zn–$I_2$ batteries. *ACS Energy Lett.* **2026**, *11*, 1117–1124.

[9] Liu, T. T.; Lei, C. J.; Yang, W.; Wang, H. J.; Ma, W. J.; Li, J. Y.; Liang, X. Solvent chemistry manipulated iodine redox thermodynamics for durable iodine batteries. *Angew. Chem., Int. Ed.* **2025**, *64*, e202422163.

[10] Weng, G. M.; Li, Z. J.; Cong, G. T.; Zhou, Y. C.; Lu, Y. C. Unlocking the capacity of iodide for high-energy-density zinc/polyiodide and lithium/polyiodide redox flow batteries. *Energy Environ. Sci.* **2017**, *10*, 735–741.

[11] Li, B.; Nie, Z. M.; Vijayakumar, M.; Li, G. S.; Liu, J.; Sprenkle, V.; Wang, W. Ambipolar zinc-polyiodide electrolyte for a high-energy density aqueous redox flow battery. *Nat. Commun.* **2015**, *6*, 6303.

[12] Zou, Y. P.; Liu, T. T.; Du, Q. J.; Li, Y. Y.; Yi, H. B.; Zhou, X.; Li, Z. X.; Gao, L. J.; Zhang, L.; Liang, X. A four-electron Zn–$I_2$ aqueous battery enabled by reversible $I^-/I_2/I^+$ conversion. *Nat. Commun.* **2021**, *12*, 170.

[13] Yue, Q.; Wan, Y.; Li, X. Q.; Zhao, Q.; Gao, T. T.; Deng, G. W.; Li, B.; Xiao, D. Restraining the shuttle effect of polyiodides and modulating the deposition of zinc ions to enhance the cycle lifespan of aqueous Zn–$I_2$ batteries. *Chem. Sci.* **2024**, *15*, 5711–5722.

[14] Huang, C. X.; Lin, H.; Xiao, F. Y.; Fang, Y. X.; Lin, C. Y.; Huang, Z. Y.; Luo, F. Q.; Yang, J. L.; Liu, Y. Y.; Qian, Q. R. et al. Micro-stepwise (100) crystal face coupling molecular-layer engineering promises high-performance Zn-iodine batteries in wide pH and seawater electrolytes. *Angew. Chem., Int. Ed.* **2026**, *65*, e6355664.

[15] Zhang, S. J.; Hao, J. N.; Li, H.; Zhang, P. F.; Yin, Z. W.; Li, Y. Y.; Zhang, B. K.; Lin, Z.; Qiao, S. Z. Polyiodide confinement by starch enables shuttle-free Zn-iodine batteries. *Adv. Mater.* **2022**, *34*, 2201716.

[16] Liu, M. M.; Chen, Q. W.; Cao, X. Y.; Tan, D. X.; Ma, J. Z.; Zhang, J. T. Physicochemical confinement effect enables high-performing zinc-iodine batteries. *J. Am. Chem. Soc.* **2022**, *144*, 21683–21691.

[17] Zhang, L. Q.; Zhang, M. J.; Guo, H. L.; Tian, Z. H.; Ge, L. F.; He, G. J.; Huang, J. J.; Wang, J. T.; Liu, T. X.; Parkin, I. P. et al. A universal polyiodide regulation using quaternization engineering toward high value-added and ultra-stable zinc-iodine batteries. *Adv. Sci.* **2022**, *9*, 2105598.

[18] Zhang, S. J.; Hao, J. N.; Wu, H.; Chen, Q. R.; Ye, C.; Qiao, S. Z. Protein interfacial gelation toward shuttle-free and dendrite-free Zn-iodine batteries. *Adv. Mater.* **2024**, *36*, 2404011.

[19] Yang, P.; Zhang, K.; Liu, S. Z.; Zhuang, W. B.; Shao, Z. P.; Zhu, K. P.; Lin, L.; Guo, G. D.; Wang, W. H.; Zhang, Q. C. et al. Ionic selective separator design enables long-life zinc-iodine batteries via synergistic anode stabilization and polyiodide shuttle suppression. *Adv. Funct. Mater.* **2024**, *34*, 2410712.

[20] Wang, G. L.; Yao, Q.; Dong, J. J.; Ge, W. J.; Wang, N. N.; Bai, Z. C.; Yang, J.; Dou, S. X. *In situ* construction of multifunctional surface coatings on zinc metal for advanced aqueous zinc-iodine batteries. *Adv. Energy Mater.* **2024**, *14*, 2303221.

[21] Xiao, T.; Yang, J. L.; Zhang, B.; Wu, J. W.; Li, J. L.; Mai, W.; Fan, H. J. All-round ionic liquids for shuttle-free zinc-iodine battery. *Angew. Chem., Int. Ed.* **2024**, *63*, e202318470.

[22] Fan, X.; Chen, L. N.; Wang, Y. J.; Xu, X. Y.; Jiao, X. X.; Zhou, P.; Liu, Y. Y.; Song, Z. X.; Zhou, J. Selection of negative charged acidic polar additives to regulate electric double layer for stable zinc ion battery. *Nano-Micro Lett.* **2024**, *16*, 270.

[23] Li, X. F.; Yu, H. M.; Alshammari, D. A.; Tian, S. Y.; Chen, G.; Xi, K.; Thabet, H. K.; Lu, B. A.; El-Bahy, Z. M.; Liu, Y. Y. et al. Regulation of proton vehicle migration for synergetic interfacial stability enables long-lasting Ah-level zinc-ion batteries. *Adv. Mater.* **2026**, *38*, e16427.

[24] Zhang, S. J.; Hao, J. N.; Wu, H.; Kao, C. C.; Chen, Q. R.; Ye, C.; Qiao, S. Z. Toward high-energy-density aqueous zinc-iodine batteries: Multielectron pathways. *ACS Nano* **2024**, *18*, 28557–28574.

[25] Chen, L. T.; Huang, S.; Feng, Z. F.; Lin, Z. X.; Huang, H. L.; Ye, M. H.; Zhang, Y. F.; Wen, Z. P.; Tang, Y. C.; Liu, X. Q. et al. Local electric field microenvironment-induced dynamic spatial confinement to stabilize $I^+$ toward high-mass-loading and stable zinc-iodine batteries. *Angew. Chem., Int. Ed.* **2025**, *64*, e202510737.

[26] Zhang, S. J.; Hao, J. N.; Wu, H.; Chen, Q. R.; Hu, Y. Y.; Zhao, X.; Qiao, S. Z. Coordination chemistry toward advanced Zn–$I_2$ batteries with four-electron $I^-/I^0/I^+$ conversion. *J. Am. Chem. Soc.* **2025**, *147*, 16350–16361.

[27] Wu, H.; Zhang, S. J.; Vongsvivut, J.; Jaroniec, M.; Hao, J. N.; Qiao, S. Z. Aqueous zinc-iodine batteries with ultra-high loading and advanced performance. *Joule* **2025**, *9*, 102000.

[28] Xiao, T.; Yang, J. L.; Xu, R. J.; Xu, H. Y.; Liu, H.; Li, J.; Bao, H. M.; Jin, X. Y.; Hwang, S. J.; Wang, Z. et al. Balanced iodophilicity and solvophilicity unlocks fast iodine conversion chemistry. *J. Am. Chem. Soc.* **2025**, *147*, 28820–28830.

[29] Zhang, L. Q.; Luo, K.; Gong, J. M.; Zhou, Y. Z.; Guo, H. L.; Yu, Y.; He, G. J.; Gohy, J. F.; Parkin, I. P.; Hofkens, J. et al. Unlocking durable and sustainable zinc-iodine batteries via molecularly engineered polyiodide reservoirs. *Angew. Chem., Int. Ed.* **2025**, *64*, e202506822.

[30] Jin, Y.; Qin, J. H.; Cao, J.; Zhang, Z. Y.; An, X.; Wang, S. H.; Yang, X. L. Fused-ring topology orchestrates crystallographic control and polyiodide sequestration for ultra-durable zinc-iodine batteries. *Energy Environ. Sci.* **2026**, *19*, 1266–1281.

[31] Liu, Y. M.; Tian, X. F.; Wang, L.; Xie, L. J.; Li, Z. C.; Ge, Y. X.; Li, Z.; Bai, Z. C.; Liu, H. K.; Wang, N. N. et al. Separator-free aqueous zinc-iodine batteries: An *in situ* dual-confinement interface enabling electrostatic reversible polyiodide capture/release. *Energy Environ. Sci.* **2026**, *19*, 2723–2734.

[32] Fu, X. R.; Pan, Y. C.; Chen, Z. X.; Li, F. L.; Yang, Y. Q.; Chen, M.; Tu, H. R.; Qiu, T. Y.; Xing, Z. Y.; Rao, P. et al. An amino acid-based functional additive enables fast polyiodide conversion kinetics for durable Zn–$I_2$ batteries. *Energy Environ. Sci.* **2026**, *19*, 1170–1179.

[33] Gong, K. P.; Du, F.; Xia, Z. H.; Durstock, M.; Dai, L. M. Nitrogen-doped carbon nanotube arrays with high electrocatalytic activity for oxygen reduction. *Science* **2009**, *323*, 760–764.

[34] Qu, L. T.; Liu, Y.; Baek, J. B.; Dai, L. M. Nitrogen-doped graphene as efficient metal-free electrocatalyst for oxygen reduction in fuel cells. *ACS Nano* **2010**, *4*, 1321–1326.

[35] Shui, J. L.; Wang, M.; Du, F.; Dai, L. M. N-doped carbon nanomaterials are durable catalysts for oxygen reduction reaction in acidic fuel cells. *Sci. Adv.* **2015**, *1*, e1400129.

[36] Guo, D. H.; Shibuya, R.; Akiba, C.; Saji, S.; Kondo, T.; Nakamura, J. Active sites of nitrogen-doped carbon materials for oxygen reduction reaction clarified using model catalysts. *Science* **2016**, *351*, 361–365.

[37] Zhao, Y.; Yang, L. J.; Chen, S.; Wang, X. Z.; Ma, Y. W.; Wu, Q.; Jiang, Y. F.; Qian, W. J.; Hu, Z. Can boron and nitrogen co-doping

improve oxygen reduction reaction activity of carbon nanotubes. *J. Am. Chem. Soc.* **2013**, *135*, 1201–1204.
[38] Wang , S.; Iyyamperumal , E.; Roy, A.; Xue, Y. H.; Yu, D. S.; Dai, L. M. Vertically aligned BCN nanotubes as efficient metal-free electrocatalysts for the oxygen reduction reaction: A synergetic effect by co-doping with boron and nitrogen. *Angew. Chem., Int. Ed.* **2011**, *50*, 11756–11760.
[39] Wang, S. Y.; Zhang, L. P.; Xia, Z. H.; Roy, A.; Chang, D. W.; Baek, J. B.; Dai, L. M. BCN graphene as efficient metal-free electrocatalyst for the oxygen reduction reaction. *Angew. Chem., Int. Ed.* **2012**, *51*, 4209–4212.
[40] Jiao, Y.; Zheng, Y.; Jaroniec, M.; Qiao, S. Z. Origin of the electrocatalytic oxygen reduction activity of graphene-based catalysts: A roadmap to achieve the best performance. *J. Am. Chem. Soc.* **2014**, *136*, 4394–4403.
[41] Hu, C. G.; Dai, L. M. Doping of carbon materials for metal-free electrocatalysis. *Adv. Mater.* **2019**, *31*, 1804672.
[42] Gao, K.; Wang, B.; Tao, L.; Cunning, B. V.; Zhang, Z. P.; Wang, S. Y.; Ruoff, R. S.; Qu, L. T. Efficient metal-free electrocatalysts from N-doped carbon nanomaterials: Mono-doping and co-doping. *Adv. Mater.* **2019**, *31*, 1805121.
[43] Kong, X. K.; Chen, C. L.; Chen, Q. W. Doped graphene for metal-free catalysis. *Chem. Soc. Rev.* **2014**, *43*, 2841–2857.
[44] Dai, L. M.; Xue, Y. H.; Qu, L. T.; Choi, H. J.; Baek, J. B. Metal-free catalysts for oxygen reduction reaction. *Chem. Rev.* **2015**, *115*, 4823–4892.
[45] Liu, X. E.; Dai, L. M. Carbon-based metal-free catalysts. *Nat. Rev. Mater.* **2016**, *1*, 16064.
[46] Chen, S. C.; Chen, Z. H.; Siahrostami, S.; Higgins, D.; Nordlund, D.; Sokaras, D.; Kim, T. R.; Liu, Y. Z.; Yan, X. Z.; Nilsson, E. et al. Designing boron nitride islands in carbon materials for efficient electrochemical synthesis of hydrogen peroxide. *J. Am. Chem. Soc.* **2018**, *140*, 7851–7859.
[47] Yang, L. J.; Jiang, S. J.; Zhao, Y.; Zhu, L.; Chen, S.; Wang, X. Z.; Wu, Q.; Ma, J.; Ma, Y. W.; Hu, Z. Boron-doped carbon nanotubes as metal-free electrocatalysts for the oxygen reduction reaction. *Angew. Chem., Int. Ed.* **2011**, *50*, 7132–7135.
[48] Yu, X. M.; Han, P.; Wei, Z. X.; Huang, L. S.; Gu, Z. X.; Peng, S. J.; Ma, J. M.; Zheng, G. F. Boron-doped graphene for electrocatalytic $N_2$ reduction. *Joule* **2018**, *2*, 1610–1622.
[49] Kong, Y.; Li, Y.; Yang, B.; Li, Z. J.; Yao, Y.; Lu, J. G.; Lei, L. C.; Wen, Z. H.; Shao, M. H.; Hou, Y. Boron and nitrogen co-doped porous carbon nanofibers as metal-free electrocatalysts for highly efficient ammonia electrosynthesis. *J. Mater. Chem. A* **2019**, *7*, 26272–26278.
[50] Huang, C. J.; Chen, C.; Zhang, M. W.; Lin, L. H.; Ye, X. X.; Lin, S.; Antonietti, M.; Wang, X. C. Carbon-doped BN nanosheets for metal-free photoredox catalysis. *Nat. Commun.* **2015**, *6*, 7698.

**Qi Xiang** is currently a master's student under the supervision of Prof. Juan Wang and Prof. Kai Xi. Her research focuses on aqueous zinc–iodine batteries, including the design of functional interlayers, the regulation of iodine redox chemistry, and the investigation of electrochemical reaction mechanisms.

**Zhengqian Jin** is a Ph.D. student at the National Energy Storage Platform of Xi'an Jiaotong University, supervised by Prof. Xi Kai. He received his B.Sc. in Chemistry and Chemical Engineering from Tongji University in 2023. His research focuses on lithium metal batteries, with emphasis on structural design, catalyst development, and material synthesis. He has authored/co-authored several papers published in journals such as *Nano-Micro Letters*, *Nano Energy*, *Advanced Materials*, and *Matter*, and has applied for several invention patents and software copyrights.

**Teng Deng** received his master's degree from Xi'an University of Architecture and Technology in 2022. Now, he is a Ph.D. candidate, under the supervision of Prof. Juan Wang and Prof. Kai Xi. His research focuses on the Li–S batteries, including the design of electrocatalysts, the design of electrolyte additives, and the analysis of reaction mechanism regulation for Li–S systems.

**Juan Wang** is currently working as a professor at Xi'an University of Architecture and Technology. She obtained her Ph.D. from Xi'an University of Architecture and Technology in 2009. Afterward, she worked as a visiting research fellow at Georgia Institute of Technology (2013–2014). Her research interests focus on energy storage materials for power sources, including Li–S battery and Li/Na/Zn-ion battery.

**Yangyang Liu** School of Instrument Science and Technology, Xi'an Jiaotong University. He was a Senior Researcher at Lomonosov Moscow State University and Moscow Institute of Physics and Technology, and Scientific Advisor at Moscow IDEA Interdisciplinary Advanced Research Center. His research focuses on interfacial chemistry and electro-mechanical evolution of solid-state batteries for device industrialization. He has published over 50 first- or corresponding-author papers including several ESI Highly Cited Papers, and serves as a reviewer for multiple international journals.

**Kai Xi** is a Professor in the School of Chemistry at Xi'an Jiaotong University, specializing in materials engineering and physical chemistry, particularly focusing on renewable energy conversion and storage technologies such as lithium-ion batteries, lithium-sulfur batteries, and solar cells. He completed his undergraduate studies in Mechanical Engineering and Automation at Xi'an Jiaotong University, and subsequently pursued further education in Applied Chemistry at Nankai University, where he obtained his master's degree. For doctoral studies, he attended the Department of Materials Science and Metallurgy at the University of Cambridge. He has published over 100 peer-reviewed papers with more than 10,000 citations and an H-index of 66 (Google Scholar as of 2026). He serves as the Guest Editor for *APL Materials* and Youth Editor for *Battery Energy*. He was awarded the grand prize of the Dow Sustainability Innovation Challenge Award.

# Electronic Supplementary Materials

# Electronegativity-programmed N-B dipolar carbon nanofiber interlayers for spatially confined iodine redox in aqueous zinc-iodine batteries

Qi Xiang[1,2,§], Zhengqian Jin[2,§], Teng Deng[1,2,§], Yaowen Yue[1,2], Kai Li[2], Minghao Xie[2], Zekai Mei[3], Hongyang Zhao[2], Juan Wang[1] (✉), Zhongxiao Song[3], Yangyang Liu[4] (✉), Shujiang Ding[2], and Kai Xi[1] (✉)

[1] *Shaanxi Key Laboratory of Nanomaterials and Nanotechnology, Xi'an Key Laboratory of Clean Energy, School of Mechanical & Electrical Engineering, Xi'an University of Architecture and Technology, Xi'an 710055, China*

[2] *School of Chemistry, Engineering Research Center of Energy Storage Materials and Devices, Ministry of Education, National Innovation Platform (Center) for Industry-Education Integration of Energy Storage Technology, State Key Laboratory of Electrical Insulation and Power Equipment, Engineering Research Center of Energy Storage Material and Chemistry, Universities of Shaanxi Province, Xi'an Jiaotong University, Xi'an 710049, China*

[3] *State Key Laboratory for Mechanical Behavior of Materials, Xi'an Jiaotong University, Xi'an 710049, China*

[4] *School of Instrument Science and Technology, Xi'an Jiaotong University, Xi'an 710049, China*

[§] *Qi Xiang, Zhengqian Jin, and Teng Deng contributed equally to this work.*

Supporting information to https://doi.org/10.26599/NRE.2026.9120270



## Experimental Section

### Materials

Polyacrylonitrile (PAN, average Mw ca. 150,000), N,N-dimethylformamide (DMF, analytical grade, ≥99.5%), urea (analytical grade, ≥99.0%), boric acid (analytical grade, ≥99.5%), hydrochloric acid (HCl, 36–38 wt%), iodine ($I_2$, ≥99.8%), zinc sulfate heptahydrate ($ZnSO_4·7H_2O$, analytical grade, ≥99.5%), polyvinylidene fluoride (PVDF), N-methyl-2-pyrrolidone (NMP, analytical grade, ≥99.5%), Super P, activated carbon, zinc foil (thickness ca. 100 μm), and commercial glass-fiber separators were used as received without further purification. Deionized water was used throughout the experiments.

All chemicals and consumables were commercially available laboratory reagents. Unless otherwise stated, all aqueous solutions were prepared using deionized water.

### Preparation of CNF

Pristine carbon nanofibers (CNF) were prepared by electrospinning followed by pre-oxidation and carbonization. Typically, 1.0 g of PAN was dissolved in 9.0 g of DMF under continuous stirring at 60 °C until a clear and homogeneous spinning solution was obtained. After ultrasonic degassing for 30 min, the PAN solution was transferred into a plastic syringe equipped with a 21 G stainless-steel needle. The electrospinning process was carried out at an applied voltage of 18 kV, a solution feed rate of 0.8 mL $h^{-1}$, and a tip-to-collector distance of 15 cm. An aluminum foil-covered collector was used to collect the PAN nanofiber membrane. The obtained PAN nanofiber membrane was dried at 60 °C

Address correspondence to Juan Wang, juanwang618@126.com; Yangyang Liu, liuyy0510@xjtu.edu.cn; Kai Xi, kx210.cam@xjtu.edu.cn

to remove residual solvent. To stabilize the fiber structure, the as-spun PAN membrane was heated to 220 °C at a heating rate of 2 °C $min^{-1}$ in air and maintained for 3 h. During this pre-oxidation process, the linear PAN chains underwent cyclization and cross-linking to form thermally stable ladder-like structures. Subsequently, the stabilized membrane was carbonized at 800 °C for 2 h under an Ar/$H_2$ mixed atmosphere (95/5, v/v) with a heating rate of 5 °C $min^{-1}$. After cooling to room temperature, the carbonized membrane was immersed in 1 M HCl for 12 h to remove residual inorganic impurities, washed repeatedly with deionized water until neutral, and vacuum-dried at 60 °C overnight to obtain pristine CNF.

**Preparation of NBCNF**

N, B co-doped carbon nanofibers (NBCNF) were prepared by introducing urea and boric acid into the PAN precursor solution before electrospinning. Typically, 1.0 g of PAN was dissolved in 9.0 g of DMF under continuous stirring at 60 °C until completely dissolved. Then, 0.30 g of urea and 0.15 g of boric acid were added as the nitrogen and boron sources, respectively. The mixture was continuously stirred at 60 °C to uniformly disperse the dopant precursors in the PAN solution. After ultrasonic degassing for 30 min, a stable and homogeneous PAN/urea/boric acid precursor spinning solution was obtained.

The precursor solution was electrospun under the same conditions as CNF, with an applied voltage of 18 kV, a solution feed rate of 0.8 mL $h^{-1}$, and a tip-to-collector distance of 15 cm. The PAN/urea/boric acid composite nanofiber membrane was collected on an aluminum foil-covered collector and then dried at 60 °C to remove residual solvent. The obtained precursor membrane was first pre-oxidized in air at 220 °C for 3 h with a heating rate of 2 °C $min^{-1}$ to prevent structural collapse during high-temperature treatment. Subsequently, the stabilized membrane was carbonized at 800 °C for 2 h under an Ar/$H_2$ mixed atmosphere (95/5, v/v) with a heating rate of 5 °C $min^{-1}$. During carbonization, the PAN framework was converted into a conductive carbon nanofiber matrix, while urea and boric acid decomposed to introduce nitrogen and boron atoms into the carbon framework in situ. The carbonized product was then immersed in 1 M HCl for 12 h, repeatedly washed with deionized water until neutral, and vacuum-dried at 60 °C overnight to obtain NBCNF. The obtained NBCNF membrane with a three-dimensional interconnected fibrous network was directly used as a functional interlayer for zinc–iodine batteries.

**Control Statement**

All electrospinning and thermal-treatment conditions for CNF and NBCNF were kept identical, except for the addition of urea and boric acid in the NBCNF precursor solution.

**Preparation of iodine cathodes**

$I_2$-loaded activated carbon ($I_2$/AC) was prepared by a thermal diffusion method. Typically, $I_2$ and

activated carbon were uniformly ground with a mass ratio of 2:1 and then heated at 90 °C for 12 h in a sealed glass vessel to allow iodine incorporation into the carbon host. After cooling to room temperature, the obtained $I_2$/AC composite was collected and used as the cathode active material.

The $I_2$/AC composite, Super P, and PVDF were mixed with a mass ratio of 8:1:1 in NMP to form a homogeneous slurry. The slurry was uniformly coated onto carbon-paper current collectors and dried at 60 °C for 12 h under vacuum. The obtained electrodes were punched into circular disks with a diameter of 12 mm. The iodine mass loading was controlled at approximately 1.0–1.5 mg $cm^{-2}$.

The specific capacity and current density of Zn–$I_2$ full cells were calculated based on the mass of iodine in the cathode unless otherwise specified. For comparison, all iodine cathodes were prepared using the same electrode formulation, coating procedure, and drying conditions.

**Cell assembly**

The NB-CNF membrane was punched into circular disks with a diameter of 16 mm. The membrane thickness was approximately 42 μm, with an areal mass loading of approximately 4.0 mg $cm^{-2}$. The electrolyte uptake was determined from the mass change of the membrane before and after soaking in 2 M $ZnSO_4$ aqueous electrolyte according to $(m_{wet} - m_{dry})/m_{dry} \times 100\%$ , and was approximately 200%. Before weighing, excess electrolyte on the membrane surface was gently removed using filter paper.

CR2032 coin cells were assembled using zinc foil as the anode, the iodine cathode as the cathode, and a glass-fiber separator as the separator. For interlayer-modified cells, the CNF or NB-CNF membrane was used as a free-standing interlayer and placed between the iodine cathode and the separator, with the interlayer in direct contact with the cathode side to regulate the migration of soluble iodine species. The electrolyte was 2 M $ZnSO_4$ aqueous solution, and the electrolyte dosage was 80 μL for each cell. The assembled cells were rested for 2 h before electrochemical testing.

**Material characterizations**

The morphology and microstructure of CNF and NB-CNF were characterized by field-emission scanning electron microscopy (FESEM) and transmission electron microscopy (TEM). The morphology of cycled Zn electrodes was examined by FESEM, and the corresponding surface roughness was analyzed by atomic force microscopy (AFM). Elemental mapping of NB-CNF was performed using energy-dispersive X-ray spectroscopy (EDS) attached to the electron-microscopy system. X-ray diffraction (XRD) patterns were collected using Cu Kα radiation (λ = 1.5406 Å) over a 2θ range of 10–80°. Fourier-transform infrared spectroscopy (FTIR) spectra were recorded in the range of 400–4000 $cm^{-1}$ to identify the bonding environments of the samples. Raman spectra were recorded using a 532 nm laser to evaluate the defect structure and graphitization degree of the carbon nanofibers. Thermogravimetric analysis (TGA), differential thermogravimetry (DTG), and differential scanning calorimetry (DSC) were conducted at a heating rate of 10 °C $min^{-1}$ to investigate the thermal behavior

of the corresponding samples. X-ray photoelectron spectroscopy (XPS) equipped with an Al Kα X-ray source was used to analyze the surface elemental composition and chemical states. Contact-angle measurements were carried out using electrolyte droplets of ca. 3 μL to evaluate the electrolyte wettability of the interlayers. The electrical resistivity of the membranes was measured using a four-point probe method.

**H-type diffusion and UV–Vis measurements**

H-type diffusion experiments were conducted to evaluate the confinement ability of CNF and NB-CNF toward soluble iodine species. Typically, the CNF or NB-CNF membrane was fixed between the two chambers of a sealed H-type cell. One chamber was filled with an iodine-containing solution consisting of 0.05 M $I_2$ in 2 M $ZnSO_4$ aqueous electrolyte, while the other chamber was filled with 2 M $ZnSO_4$ aqueous electrolyte. The solution volumes in the two chambers were kept identical. The color change of the receiving chamber was recorded at 0, 15, 30, and 60 min. At selected time intervals, aliquots from the receiving chamber were collected and analyzed by UV–Vis spectroscopy over a wavelength range of 250–500 nm to monitor the diffusion of soluble iodine species.

**Electrochemical measurements**

Galvanostatic charge–discharge tests, rate performance, long-term cycling, and self-discharge measurements were performed using a multichannel battery testing system at room temperature. The voltage window for Zn–$I_2$ full cells was 0.6–1.6 V. Rate performance was tested at 1, 2, 5, 10, 20, and 50 C, where 1 C corresponds to 211 mA $g^{-1}$ based on the theoretical capacity of iodine. Long-term cycling was conducted at 10 C, and additional cycling tests were conducted at 1 C. For self-discharge tests, the cells were first charged to 1.6 V, rested for 48 h, and then discharged at the same current density to evaluate the capacity retention.

Cyclic voltammetry (CV) and electrochemical impedance spectroscopy (EIS) were carried out on an electrochemical workstation at room temperature. CV curves were recorded at scan rates from 0.2 to 1.0 mV $s^{-1}$ within the same voltage window as the galvanostatic tests. EIS spectra were collected after resting at open-circuit voltage over a frequency range of 100 kHz to 0.01 Hz with a perturbation amplitude of 5 mV. The capacitive-controlled and diffusion-controlled current contributions were separated according to:

$$i(V)=k_1v+k_2v^{1/2}$$

where i(V) is the current response at a given potential V,v is the scan rate, $k_1v$ represents the capacitive-controlled contribution, and $k_2v^{1/2}$ represents the diffusion-controlled contribution. The equation can be rearranged as:

$$i(V)/v^{1/2}=k_1v^{1/2}+k_2$$

At each potential, $k_1$ and $k_2$ were obtained by linear fitting of $i(V)/v^{1/2}$ versus $v^{1/2}$ using the CV curves collected at different scan rates. The capacitive-controlled and diffusion-controlled current components were then calculated as $k_1v$ and $k_2v^{1/2}$, respectively, and their relative contributions were determined by integrating the corresponding current components over the investigated potential window.

Zn//Zn symmetric cells were assembled to evaluate Zn plating/stripping stability. The same 16-mm-diameter NB-CNF membranes described above were used for the Zn//Zn symmetric cells. For interlayer-modified Zn//Zn cells, CNF or NB-CNF membranes were placed between the two Zn foils as interfacial regulation layers. The symmetric cells were tested in 2 M $ZnSO_4$ aqueous electrolyte at 1 mA $cm^{-2}$/1 mAh $cm^{-2}$ and 5 mA $cm^{-2}$/5 mAh $cm^{-2}$. After cycling, the Zn electrodes were carefully disassembled, gently rinsed with deionized water and ethanol to remove residual electrolyte, dried, and characterized by SEM and AFM.

**Theoretical calculations**

All density functional theory (DFT) calculations were performed using the Vienna Ab initio Simulation Package (VASP)[1] with the projector-augmented wave (PAW)[2] method. The Perdew-Burke-Ernzerhof (PBE) functional within the generalized gradient approximation (GGA) was employed to describe the exchange-correlation interactions[3], together with Grimme's DFT-D3 dispersion correction with zero damping. The plane-wave basis set was expanded to a kinetic-energy cutoff of 500 eV. All models were built in a 4 × 4 graphene supercell (a = b = 9.84 Å, γ = 120°) with a cell height of c = 20.80 Å, which leaves a vacuum spacing of more than 15 Å along the surface normal between periodic images. The Brillouin zone was sampled with a Γ-centred Monkhorst-Pack[4] 3 × 3 × 1 k-point mesh, and partial occupancies were treated by Gaussian smearing with a width of σ = 0.05 eV. All atomic positions were relaxed at fixed cell parameters until the total energy converged to within 1 × 10−5 eV and all residual forces were smaller than 0.02 eV Å−1. The calculations were spin-restricted. The charged iodine species were treated as genuine anions by adding one electron to the calculation (NELECT = Nval + 1), with the resulting net charge of −1 e compensated by a uniform neutralizing background; the corresponding adsorption complexes were computed with the same net charge in the same supercell, so that the adsorption process is charge-balanced.

Carbon models containing pyrrolic-N, pyridinic-N, pyrrolic N/B, and pyridinic N/B sites were constructed, and the adsorption behaviors of $I^-$ and $I_3^-$ species were compared. The adsorption energy was calculated as

$$E_{\text{ads}} = E_{\text{substrate+adsorbate}} - E_{\text{substrate}} - E_{\text{adsorbate}}$$

where Esubstrate+adsorbate is the total energy of the fully relaxed adsorption complex, Esubstrate is the total energy of the fully relaxed, charge-neutral N-doped or N/B co-doped graphene supercell in the absence of any adsorbate, and Eadsorbate is the total energy of the relaxed, isolated iodine species ($I_2$, $I^-$ or $I_3^-$) computed in the same supercell and with the same numerical settings — charge-neutral for $I_2$, and with one added electron and a compensating neutralizing background for the anions, as described above. Total density of states (TDOS) calculations were further performed to compare the electronic structures of N-doped and N/B co-doped carbon models.

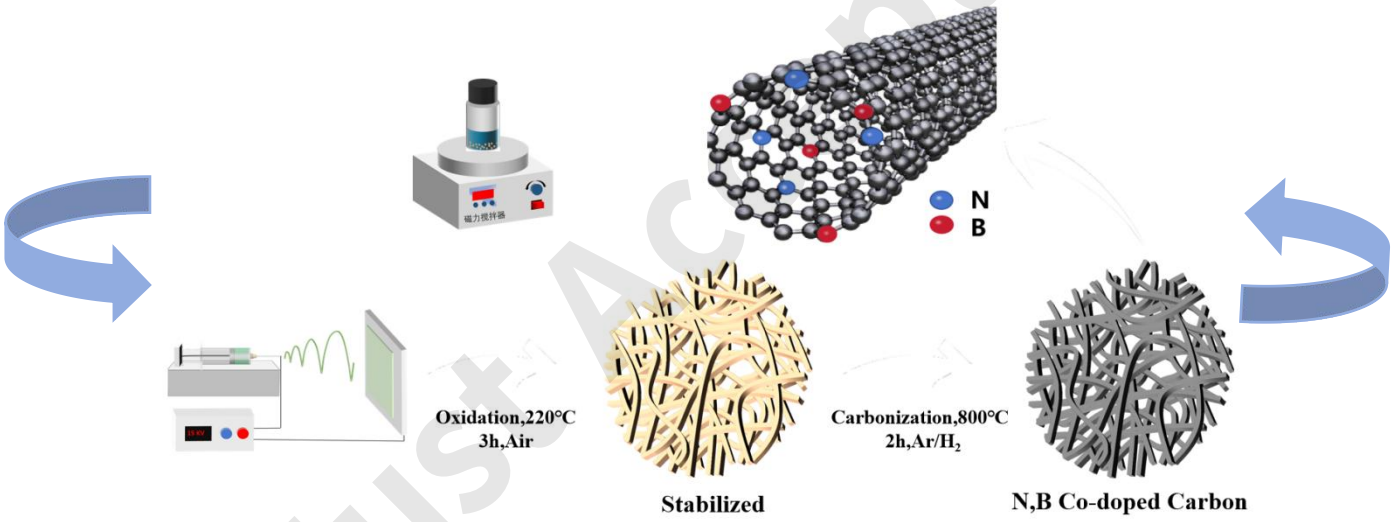


Figure S1. Schematic illustration of the preparation of NB-CNF through electrospinning, preoxidation, and carbonization.

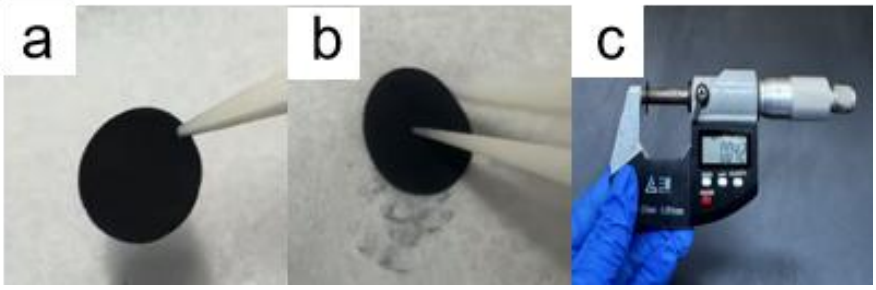


Figure S2. Optical photographs of the NB-CNF membrane. (a,b) Flexibility of the self-standing NB-CNF membrane under bending and handling. (c) Thickness measurement of the NB-CNF membrane.

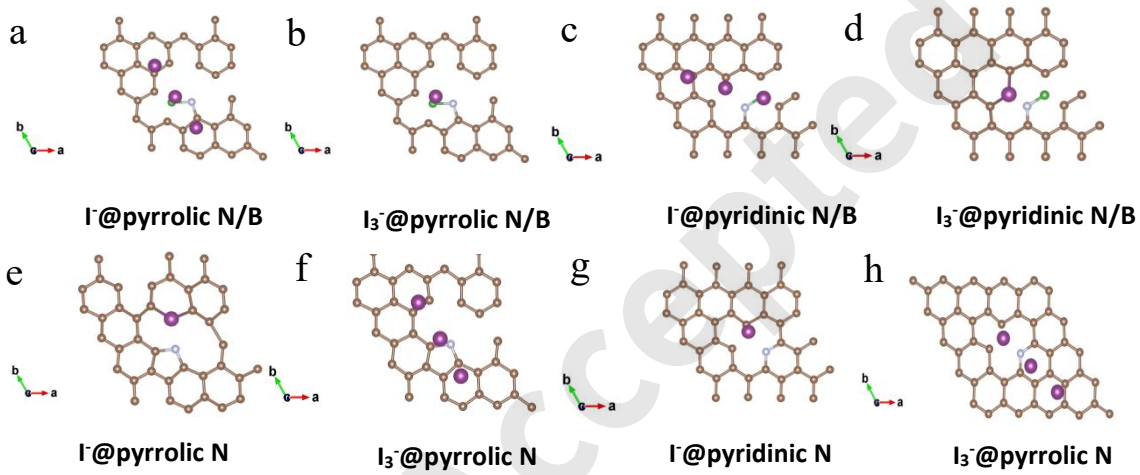


Figure S3. Optimized adsorption configurations of iodine species on N-doped and N/B co-doped carbon sites. (a,b) $I^-$ and $I_3^-$ adsorption on pyrrolic N/B sites, respectively. (c,d) $I^-$ and $I_3^-$ adsorption on pyridinic N/B sites, respectively. (e,f) $I^-$ and $I_3^-$ adsorption on pyrrolic N sites, respectively. (g,h) $I^-$ and $I_3^-$ adsorption on pyridinic N sites, respectively.

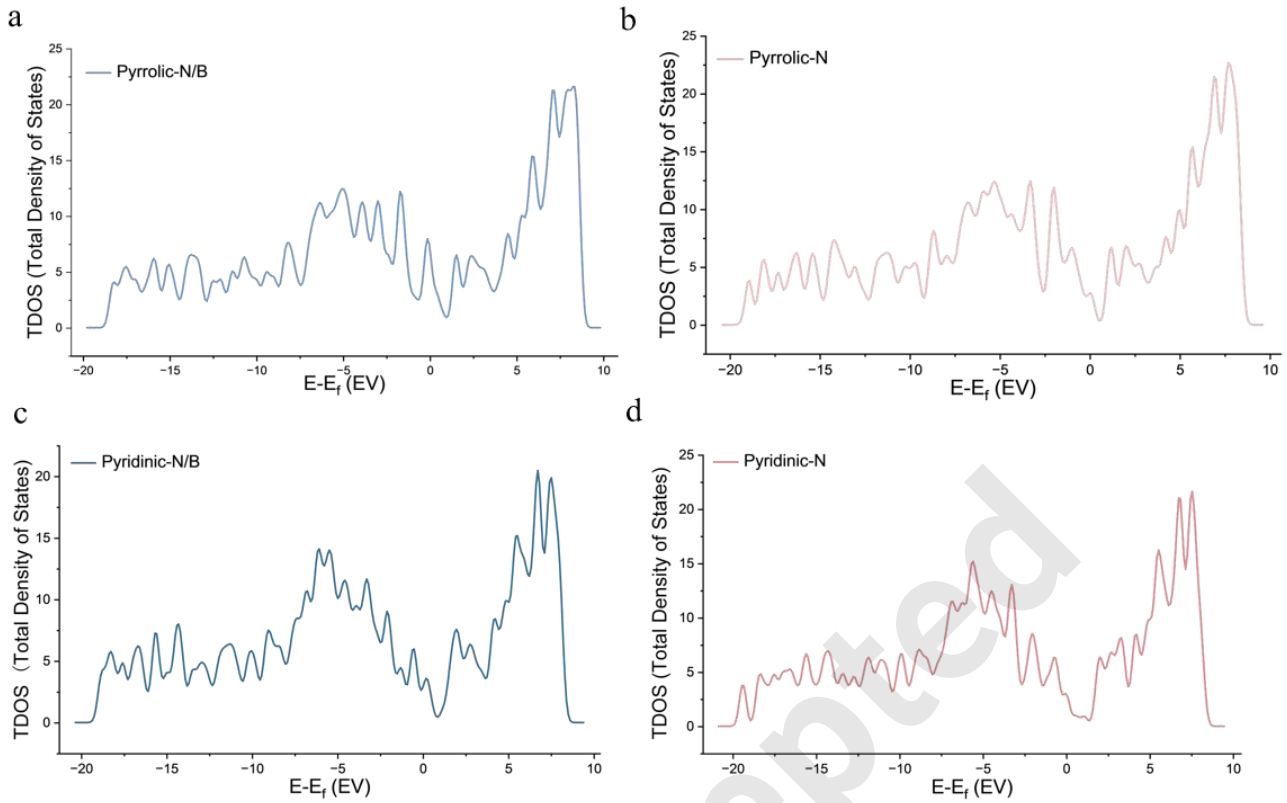


Figure S4. Total density of states (TDOS) of N-doped and N/B co-doped carbon structures. (a) Pyrrolic N/B co-doped carbon. (b) Pyrrolic N-doped carbon. (c) Pyridinic N/B co-doped carbon. (d) Pyridinic N-doped carbon.



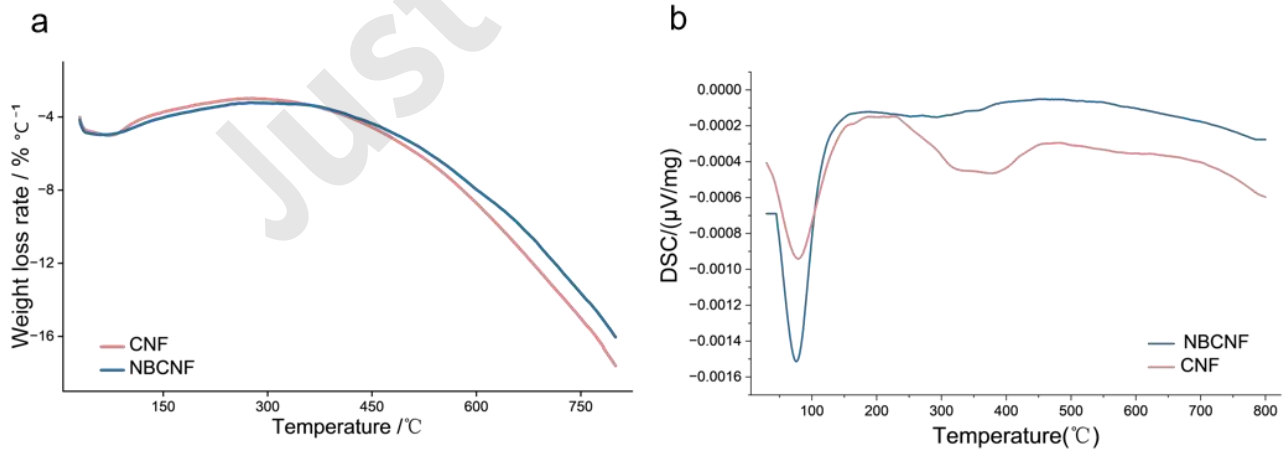


Figure S5. Thermal analysis of CNF and NB-CNF precursors. (a) DTG curves of CNF and NB-CNF precursors. (b) DSC curves of CNF and NB-CNF precursors.

## References


[1] Blöchl, P. E. Projector augmented-wave method. *Physical review B* **1994**, *50*, 17953.

[2] Kresse, G.; Joubert, D. From ultrasoft pseudopotentials to the projector augmented-wave method. *Physical review b* **1999**, *59*, 1758.

[3] Perdew, J. P.;Burke, K.; Ernzerhof, M. Generalized gradient approximation made simple. *Phys. Rev. Lett.* **1996**, *77*, 3865.

[4] Monkhorst, H. J.; Pack, J. D. Special points for Brillouin-zone integrations. *Physical review B* **1976**, *13*, 5188.